A programmable two-qubit quantum processor in silicon

Watson, T. F.; Philips, S. G.J.; Kawakami, E.; Ward, D. R.; Scarlino, P.; Veldhorst, M.; Savage, D. E.; Lagally, M. G.; Friesen, Mark; Coppersmith, S. N.

DOI
10.1038/nature25766

Publication date
2018

Document Version
Final published version

Published in
Nature

Citation (APA)
Watson, T. F., Philips, S. G. J., Kawakami, E., Ward, D. R., Scarlino, P., Veldhorst, M., Savage, D. E., Lagally, M. G., Friesen, M., Coppersmith, S. N., Eriksson, M. A., & Vandersypen, L. M. K. (2018). A programmable two-qubit quantum processor in silicon. *Nature*, *555*(7698), 633-637. https://doi.org/10.1038/nature25766

LETTER

doi:10.1038/nature25766

A programmable two-qubit quantum processor in silicon

T. F. Watson[1], S. G. J. Philips[1], E. Kawakami[1], D. R. Ward[2], P. Scarlino[1], M. Veldhorst[1], D. E. Savage[2], M. G. Lagally[2], Mark Friesen[2], S. N. Coppersmith[2], M. A. Eriksson[2] & L. M. K. Vandersypen[1]

Now that it is possible to achieve measurement and control fidelities for individual quantum bits (qubits) above the threshold for fault tolerance, attention is moving towards the difficult task of scaling up the number of physical qubits to the large numbers that are needed for fault-tolerant quantum computing[1,2]. In this context, quantum-dot-based spin qubits could have substantial advantages over other types of qubit owing to their potential for all-electrical operation and ability to be integrated at high density onto an industrial platform[3–5]. Initialization, readout and single- and two-qubit gates have been demonstrated in various quantum-dot-based qubit representations[6–9]. However, as seen with small-scale demonstrations of quantum computers using other types of qubit[10–13], combining these elements leads to challenges related to qubit crosstalk, state leakage, calibration and control hardware. Here we overcome these challenges by using carefully designed control techniques to demonstrate a programmable two-qubit quantum processor in a silicon device that can perform the Deutsch–Josza algorithm and the Grover search algorithm—canonical examples of quantum algorithms that outperform their classical analogues. We characterize the entanglement in our processor by using quantum-state tomography of Bell states, measuring state fidelities of 85–89 per cent and concurrences of 73–82 per cent. These results pave the way for larger-scale quantum computers that use spins confined to quantum dots.

Solid-state approaches to quantum computing are challenging to realize owing to unwanted interactions between the qubit and the host material. For quantum-dot-based qubits, charge and nuclear-spin noise are the dominant sources of decoherence and gate errors. Some of these effects can be cancelled out by using dynamical decoupling[14] or decoherence-free subspaces[9,15], but there has also been substantial progress in reducing these noise sources by growing better oxides and heterostructures[16] and moving to silicon, owing to its naturally low abundance of nuclear-spin isotopes that can be removed through isotopic purification[17]. These material developments have greatly extended the coherence times of qubits, enabling single-qubit gate fidelities of above 99%[18–21], and recently resulted in the demonstration of a controlled-phase (CZ) gate between two single-electron-spin qubits in a silicon metal–oxide–semiconductor (Si-MOS) device[8]. Here, we show that with two single-electron-spin qubits in a natural silicon/silicon germanium (Si/SiGe) double quantum dot we can combine initialization, readout, single- and two-qubit gates to form a programmable quantum processor in silicon that can perform simple quantum algorithms.

A schematic of the two-qubit quantum processor is shown in Fig. 1a. The device is similar to that described previously[22] except for an additional micrometre-scale magnet ('micromagnet'). A two-dimensional electron gas is formed in the natural silicon quantum well of a SiGe heterostructure using two accumulation gates. The double quantum dot is defined in this two-dimensional electron gas by applying negative voltages to the depletion gates, with the estimated positions of the first (D1) and second (D2) quantum dot shown by the purple and orange circles, respectively. The two qubits, Q1 and Q2, are defined by applying a finite magnetic field $B_{ext} = 617$ mT and using the Zeeman-split spin-down $|0\rangle$ and spin-up $|1\rangle$ states of single electrons, respectively, which are confined in D1 and D2. The initialization and readout of Q2 are performed by spin-selective tunnelling to a reservoir[23], while Q1 is initialized at a spin-relaxation hotspot[24] and measured via Q2 using a controlled-rotation (CROT) gate. The complete measurement sequence and set-up are described in Extended Data Figs 1 and 2. We achieve initialization ('I' subscript) and readout ('m' subscript) fidelities for the two qubits of $F_{I1} > 99\%$, $F_{I2} > 99\%$, $F_{m1} = 73\%$ and $F_{m2} = 81\%$ (see Methods).

The coherent individual control of both qubits is achieved by patterning three cobalt micromagnets on top of the device (Fig. 1a). These micromagnets provide a magnetic-field gradient with a component that is perpendicular to the external magnetic field for electric dipole spin resonance (EDSR)[25]. Furthermore, the field gradient across the two dots results in qubit frequencies that are well separated ($f_{Q1} = 18.4$ GHz, $f_{Q2} = 19.7$ GHz), which allows the qubits to be addressed independently. For both qubits, we achieve Rabi frequencies of $f_R = \omega_R/(2\pi) = 2$ MHz and perform single-qubit X and Y gates by using vector modulation of the microwave drive signals. Here, we define an X (Y) gate to be a $\pi/2$ rotation around $\hat{x}$ ($\hat{y}$), and henceforth define a π rotation to be X^2 (Y^2). We measure the spin relaxation time (T_1), free evolution time (T_2^*) and the Hahn echo decay time (T_{2Hahn}) of Q1 in the (1, 1) regime (where (m, n) denotes a configuration with m electrons in D1 and n electrons in D2) to be $T_1 > 50$ ms, $T_2^* = 1.0 \pm 0.1$ μs and $T_{2Hahn} = 19 \pm 3$ μs, and those of Q2 to be $T_1 > 3.7 \pm 0.5$ ms, $T_2^* = 0.6 \pm 0.1$ μs and $T_{2Hahn} = 7 \pm 1$ μs (Extended Data Fig. 3). Using randomized benchmarking[20,26] we find average single-qubit gate fidelities of 98.8% for Q1 and 98.0% for Q2 (Extended Data Fig. 4)—close to the fault-tolerance error threshold for surface codes[27].

Universal quantum computing requires the implementation of single- and two-qubit gates. In our quantum processor we implement a two-qubit CZ gate[8,28]. This gate can be understood by considering the energy-level diagram for two electron spins in a double quantum dot (Fig. 1b), in the regime in which the Zeeman-energy difference is comparable to the inter-dot tunnel coupling ($\Delta E_Z \approx t_c$). In Fig. 1b we plot the energies of the two-spin states ($|00\rangle$, $|01\rangle$, $|10\rangle$ and $|11\rangle$) in the (1, 1) charge regime and the singlet ground state S(0, 2) in the (0, 2) charge regime as a function of the detuning ε. Here, detuning describes the energy difference between the (1, 1) and (0, 2) charge states of the double quantum dot, controlled by the voltage applied to plunger gate P1 (Extended Data Fig. 2). The anticrossing between the S(0, 2) and the antiparallel $|01\rangle$ and $|10\rangle$ states causes the energy of the antiparallel states to decrease by $J(\varepsilon)/2$ as the detuning is decreased (Fig. 1b), where $J(\varepsilon)$ is the exchange coupling between the two electron spins.

The energy structure of the two-electron system can be probed by performing microwave spectroscopy as a function of detuning (Fig. 1c). At negative detuning, the resonance frequency (Zeeman energy) increases linearly (dashed line) owing to the electron

[1]QuTech and the Kavli Institute of Nanoscience, Delft University of Technology, 2600 GA Delft, The Netherlands. [2]University of Wisconsin-Madison, Madison, Wisconsin 53706, USA.

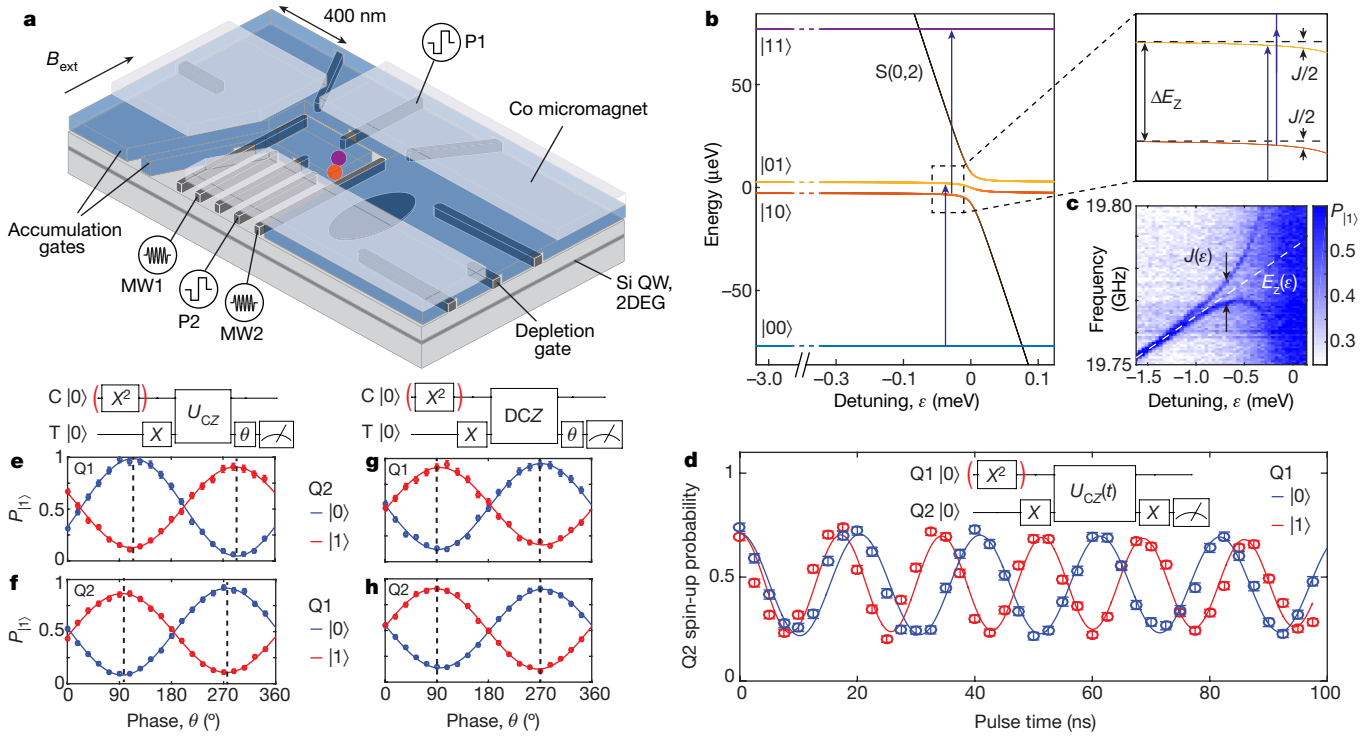

Figure 1 | Two-qubit quantum processor in silicon. a, Schematic of a Si/SiGe double-quantum-dot device, showing the estimated positions of quantum dots D1 (purple circle) and D2 (orange circle) that are used to confine two electron-spin qubits Q1 and Q2, respectively. Both quantum dots were formed from the two-dimensional electron gas (2DEG) in the silicon quantum well (Si QW) on the right side of the device to achieve an inter-dot tunnel coupling that is suitable for two-qubit gates. The positions of the dots were realized by tuning the numerous accumulation and depletion gates, but were probably helped by disorder in the Si/SiGe heterostructure. The ellipse shows the position of the quantum-dot sensor used for spin readout. Microwave signals MW1 and MW2 are used to perform electric dipole spin resonance (EDSR), mediated by the cobalt (Co) micromagnets, on Q1 and Q2, respectively, while voltage pulses are applied to plunger gates P1 and P2 for qubit manipulation and readout. **b**, Energy-level diagram of two electron spins in a double quantum dot as a function of the detuning energy ε between the (1, 1) and (0, 2) charge states. Towards zero detuning the energy levels of the anti-parallel spin states shift by half the exchange energy J (see inset) **c**, Microwave spectroscopy of Q2 showing the spin-up probability $P_{|1\rangle}$ versus the MW2 frequency and detuning energy after initialization of Q1 to $(|0\rangle + |1\rangle)/\sqrt{2}$. The detuning voltage was converted to energy using a lever arm of $\alpha = 0.09e$, where e is the electron charge (Extended Data Fig. 5). The map shows that Q2 has two different resonant frequencies (blue arrows in **b**) depending on the spin state of Q1, which are separated by the exchange energy J. **d**, The spin-up probability of Q2 after applying the Ramsey sequence (see inset) in which the duration of the detuning pulse is varied between two X gates on Q2, and the control Q1 is initialized to spin-down (blue curve) or spin-up (red curve). **e**, The spin-up probability of the target qubit (T; Q1) after applying the Ramsey sequence shown above the plot, in which a CZ gate is applied between two $\pi/2$ pulses and the phase of the second $\pi/2$ pulse is varied. Here, the control (C) qubit (C; Q2) is initialized to spin-down (blue curve) or spin-up (red curve) and the spin-up probability has been normalized to remove initialization and readout errors. The exchange energy during the CZ gate is $J/h = 10$ MHz. **f**, Similar to **e**, but with Q2 as the target qubit and Q1 as the control qubit. In **e** and **f**, the black dashed lines show the $\hat{z}$ rotations on Q1 and Q2 that are needed to form the CZ_{ij} gates. **g**, **h**, Similar to **e** and **f**, but using a decoupled version of the CZ gate (DCZ gate), which removes the unconditional $\hat{z}$ rotations due to the detuning dependence of $E_Z(\varepsilon)$. Consequently, the $\hat{z}$ rotations that are required to form the CZ_{ij} gates (dashed black lines) are always at 90° and 270°, which simplifies the calibration. All error bars are 1σ from the mean, calculated using a Monte Carlo method (see Methods).

wavefunction moving in the magnetic-field gradient. At more positive detuning, closer to the (0, 2) regime, the exchange energy is substantial compared to the line width of the resonance $J/h > \omega_R$ (where $h = 2\pi\hbar$ is the Planck constant), resulting in two clear resonances. Applying a π pulse at one of these frequencies results in a CROT gate, which is used to perform the projective measurement of Q1 via the readout of Q2 (Extended Data Fig. 6).

The CZ gate is implemented by applying a detuning pulse for a fixed amount of time t, which shifts the energy of the antiparallel states. Throughout the pulse, we stay in the regime in which $J(\varepsilon) \ll \Delta E_Z$, so the energy eigenstates of the system are still the two-spin product states and the two-qubit interaction can be approximated by an Ising Hamiltonian, leading to the following unitary operation:

$$U_{CZ}(t) = Z_1(\theta_1)Z_2(\theta_2)\begin{pmatrix} 1 & 0 & 0 & 0 \\ 0 & e^{iJ(\varepsilon)t/(2\hbar)} & 0 & 0 \\ 0 & 0 & e^{iJ(\varepsilon)t/(2\hbar)} & 0 \\ 0 & 0 & 0 & 1 \end{pmatrix} \quad (1)$$

where the basis states are $|00\rangle$, $|01\rangle$, $|10\rangle$ and $|11\rangle$, and $Z_1(\theta_1)$ and $Z_2(\theta_2)$ are rotations around $\hat{z}$ caused by the change in the Zeeman energy of the qubits due to the magnetic-field gradient. The CZ gate is advantageous over the CROT gate because it is faster and less time is spent at low detuning, at which the qubits are more sensitive to charge noise. In addition, we observed that performing the CROT gate with EDSR can lead to state leakage into the S(0, 2) state, seen in Fig. 1c by the increase in background dark counts near $\varepsilon = 0$. The CZ gate is demonstrated in Fig. 1d; we vary the duration of a CZ voltage pulse between two X gates on Q2 in a Ramsey experiment, showing that the frequency of the $\hat{z}$ rotation on Q2 is conditional on the spin state of Q1. The processor's primitive two-qubit gates, $CZ_{ij}|m, n\rangle = (-1)^{\delta(i,m)\delta(j,n)}|m, n\rangle$ for i, j, m, $n \in \{0, 1\}$, are constructed by applying the CZ gate for a time $t = \pi\hbar/J$ followed by $\hat{z}$ rotations on Q1 and Q2, $CZ_{ij} = Z_1[(-1)^j\pi/2 - \theta_1]Z_2[(-1)^i\pi/2 - \theta_2]U_{CZ}(\pi\hbar/J)$. Rather than physically performing the $\hat{z}$ rotations, we change the reference frame in the software by incorporating the rotation angles θ_1 and θ_2 into the phase of any subsequent microwave pulses[10].

Combining single- and two-qubit gates together with initialization and readout, we demonstrate a programmable processor—whereby we can program arbitrary sequences for the two-qubit chip to execute within the coherence times of the qubits. To achieve this, several challenges needed to be overcome. The device had to be tuned further so that during single-qubit gates the exchange coupling was low ($J_{off}/h = 0.27$ MHz; Extended Data Fig. 7) compared to our single-qubit (about 2 MHz) and two-qubit (about 6–10 MHz) gate times. Tuning was also required to raise the energy of low-lying valley-excited states to prevent them from being populated during initialization[22]. Furthermore, we observed that applying microwave pulses on Q1 shifts the resonance frequency of Q2 by around 2 MHz. We rule out the AC Stark shift and effects from coupling between the spins and from heating as possible explanations, but find that the properties of the quantum dots affect the frequency shift (Supplementary Information, section S1). Although the origin of the shift is unknown, we keep the resonance frequency of Q2 fixed during single-qubit gates by applying an off-resonant pulse (30 MHz) to Q1 if Q1 is idle.

Before running sequences on the quantum processor, all gates need to be properly calibrated. The single-qubit X and Y gates were calibrated using both a Ramsey sequence and the AllXY calibration sequence to determine the qubit resonance frequency and the power needed to perform a $\pi/2$ gate (Supplementary Information, section S2). To calibrate the CZ_{ij} gates we performed the Ramsey sequence shown in Fig. 1e and varied the phase of the second $\pi/2$ gate. In Fig. 1e we show the results of this measurement, for which Q1 is the target qubit and the control qubit Q2 is prepared in either the $|0\rangle$ (blue curve) or $|1\rangle$ (red curve) state. The duration of the CZ gate is calibrated so that the blue and red curves are 180° out of phase. These measurements also determine the $\hat{z}$ rotation on Q1 that is needed to form CZ_{ij}, which corresponds to the phase of the second $\pi/2$ gate, which either maximizes or minimizes the spin-up probability for Q2 (dashed lines in Fig. 1e). The $\hat{z}$ rotation needed for Q2 is calibrated by performing a similar measurement, but with the roles of Q1 and Q2 switched (Fig. 1f).

The $\hat{z}$ rotations in equation (1) can be eliminated by using a decoupled CZ gate, $\mathrm{DCZ} = U_{CZ}(\pi\hbar/(2J))X_1^2X_2^2U_{CZ}(\pi\hbar/(2J))$, which incorporates refocusing pulses and can be used to perform $\mathrm{DCZ}_{ij} = X_1^2X_2^2CZ_{ij} = Z_1[(-1)^j\pi/2]Z_2[(-1)^i\pi/2]\mathrm{DCZ}$. This operation is demonstrated in the Ramsey experiment shown in Fig. 1g, h, in which the minimum and maximum spin-up probabilities occur at a phase of either 90° or 270°. In addition to removing the need to calibrate the required $\hat{z}$ rotations, the DCZ gate is advantageous because it cancels out the effect of the low-frequency noise that couples to the spins via $\sigma_Z \otimes I$ and $I \otimes \sigma_Z$ terms during the implementation of the gate, where I is the 2×2 identity matrix and σ_Z is the Pauli z matrix.

After proper calibration, we characterize entanglement in our quantum processor by preparing Bell states and reconstructing the two-qubit density matrix using quantum-state tomography. The quantum circuit for the experiment is shown in Fig. 2a. The Bell states are prepared using a combination of single-qubit gates and the decoupled two-qubit DCZ_{ij} gates. The density matrix is reconstructed by measuring two-spin probabilities for the nine combinations of three different measurement bases (x, y, z) with 10,000 repetitions (Methods). In our readout scheme the states are projected into the z basis, while measurements in the other bases are achieved by performing X and Y pre-rotations. Owing to the time needed to perform these measurements (about 2 h), the frequency of the qubits was calibrated after every 100 repetitions. The real components of the reconstructed density matrices of the four Bell states $((|00\rangle \pm |11\rangle)/\sqrt{2}, (|01\rangle \pm |10\rangle)\sqrt{2})$ are shown in Fig. 2b–e. The state fidelities $F = \langle\psi|\rho|\psi\rangle$ between the measured density matrix (ρ) and the target Bell state (ψ) range from 85% to 89% and the concurrences from 73% to 82%, demonstrating entanglement. A parallel experiment reported a Bell-state fidelity of 78%[29].

To test the programmability of the two-qubit quantum processor we perform the Deutsch–Josza[30] and Grover search[31] quantum algorithms.

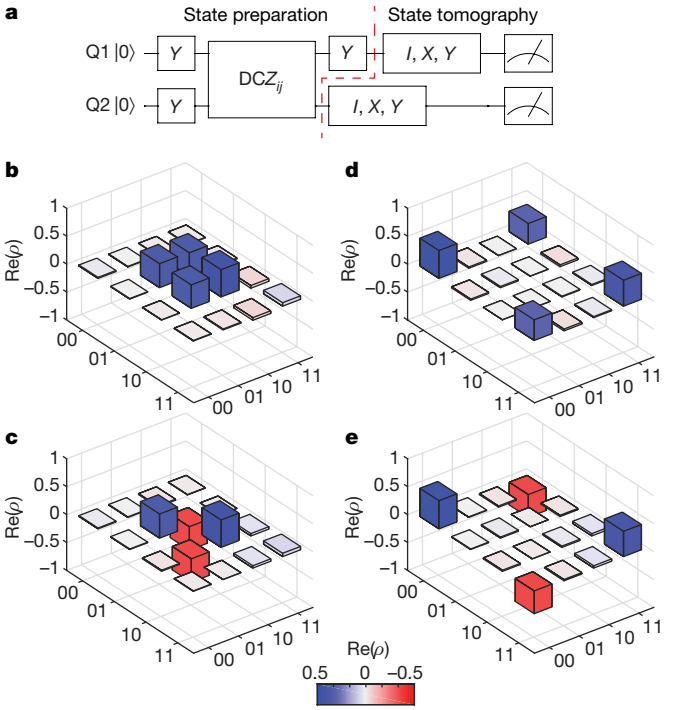

Figure 2 | Preparation of the Bell states and two-qubit entanglement in silicon. a, The quantum circuit used to prepare the Bell states and to perform quantum state tomography. The Bell states are prepared using a combination of single-qubit Y gates and two-qubit DCZ_{ij} gates while quantum-state tomography is performed by using different combinations of I, X and Y pre-rotation gates, where I corresponds to the identity. **b**–**e**, The real component of the reconstructed density matrices (Re(ρ)), determined using a maximum-likelihood estimate for the four Bell states $\Psi^+ = (|01\rangle + |10\rangle)/\sqrt{2}$ (**b**), $\Psi^- = (|01\rangle - |10\rangle)/\sqrt{2}$ (**c**), $\Phi^+ = (|00\rangle + |11\rangle)/\sqrt{2}$ (**d**), $\Phi^- = (|00\rangle - |11\rangle)/\sqrt{2}$ (**e**). The imaginary components of the elements of the density matrices are less than 0.08 in all cases (Supplementary Information, section S3). We measure state fidelities of $F_{\Psi^+} = 0.88 \pm 0.02$, $F_{\Psi^-} = 0.88 \pm 0.02$, $F_{\Phi^+} = 0.85 \pm 0.02$ and $F_{\Phi^-} = 0.89 \pm 0.02$, and concurrences of $c_{\Psi^+} = 0.80 \pm 0.03$, $c_{\Psi^-} = 0.82 \pm 0.03$, $c_{\Phi^+} = 0.73 \pm 0.03$ and $c_{\Phi^-} = 0.79 \pm 0.03$; all errors are 1σ from the mean.

The Deutsch–Josza algorithm determines whether a function is constant ($f_1(0) = f_1(1) = 0$ or $f_2(0) = f_2(1) = 1$) or balanced ($f_3(0) = 0$, $f_3(1) = 1$ or $f_4(0) = 1$, $f_4(1) = 0$). These four functions are mapped onto the unitary operators $U_{f_1} = I, U_{f_2} = X_2^2, U_{f_3} = \mathrm{CNOT} = Y_2CZ_{11}\overline{Y}_2$ and $U_{f_4} = \text{Z-CNOT} = \overline{Y}_2CZ_{00}Y_2$, where the overbar denotes a negative rotation. For both the controlled-NOT (CNOT) and the zero-controlled-NOT (Z-CNOT) gates, the target qubit is Q2. At the end of the sequence the input qubit (Q1) will be in the $|0\rangle$ or $|1\rangle$ state for the constant and balanced functions, respectively. Grover's search algorithm provides an optimal method for finding the unique input value x_0 of a function $f(x)$ that gives $f(x_0) = 1$ and $f(x) = 0$ for all other values of x. In the two-qubit version of this algorithm there are four input values, $x \in \{00, 01, 10, 11\}$, resulting in four possible functions $f_{ij}(x)$, with $i, j \in \{0, 1\}$. These functions are mapped onto the unitary operators, $CZ_{ij}|x\rangle = (-1)^{f_{ij}(x)}|x\rangle$, which mark the input state with a negative phase if $f_{ij}(x) = 1$. The algorithm finds the state that has been marked and outputs it at the end of the sequence.

In Fig. 3 we show the measured two-spin probabilities as a function of time during the algorithms for each function. The experimental results (circles) are in good agreement with the simulated ideal cases (dashed lines). Although a number of repetitions are needed as a result of gate and readout errors, the algorithms are successful at determining the balanced and constant functions and finding the marked state in the oracle functions. The data shown as square symbols are taken shortly after calibration and are in line with the experimental results (circles),

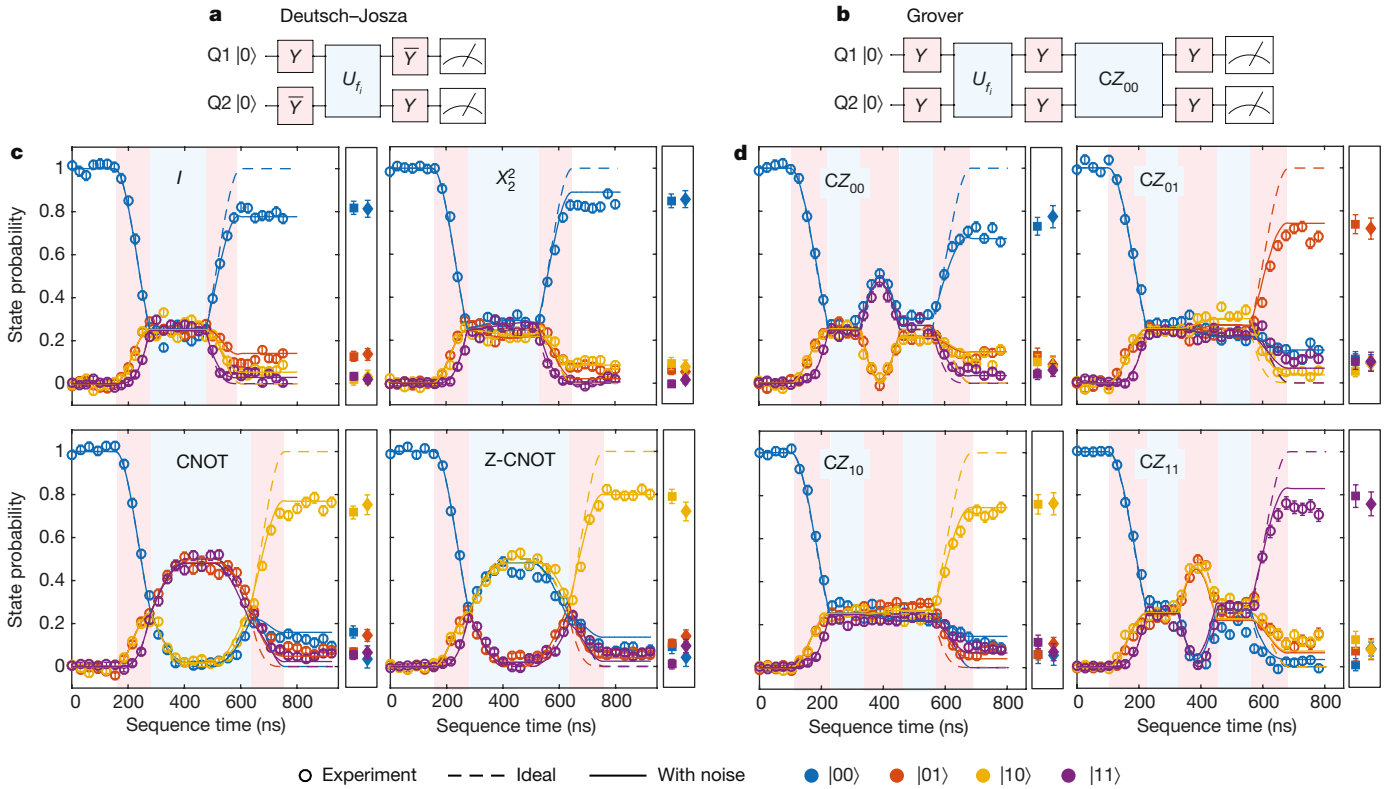

Figure 3 | Two-qubit quantum algorithms in silicon. a, **b**, Quantum circuits showing the sequences of single- and two-qubit gates that were applied for the Deutsch–Josza algorithm (**a**) and the Grover search algorithm (**b**) for two qubits. The Deutsch–Josza algorithm determines whether the function U_f is constant or balanced; the Grover search algorithm finds the state marked by the function U_f. **c**, **d**, Two-spin probabilities as a function of time throughout the sequence during the Deutsch–Josza algorithm (**c**) and the Grover search algorithm (**d**), for each of four possible functions. Each experimental data point (circles) corresponds to 4,000 repetitions and has been normalized to remove readout errors. The dashed lines are the simulated ideal cases and the solid lines are the simulated results when decoherence is introduced by including quasi-static nuclear-spin and charge noise ($\sigma_\varepsilon = 11\,\mu$eV). For both algorithms, the square data points show the final results of the algorithms when all four functions are evaluated in the same measurement run with identical calibration. The diamonds show the result of both algorithms when using the DC*Z* gate, demonstrating similar performance to the C*Z* gate. For the Deutsch–Josza algorithm, the identity I is implemented as either a 200-ns wait (circles and squares) or as $I = X_1^4 X_2^4$ (diamonds). All error bars are 1σ from the mean. The red and blue shading in **c** and **d** corresponds to that in **a** and **b**.

indicating that calibrations remain stable throughout the hour of data collection. The diamonds show the outcome of the algorithms using the DC*Z* gate. In most cases, the diamonds also show similar values to the circles, which means that the DC*Z* gate does not improve the final result. This suggests that low-frequency single-qubit noise during the C*Z* gate is not dominant. The substantial difference between Hahn-echo and Ramsey decay times still points to substantial low-frequency noise. Single-qubit low-frequency noise, whether from nuclear-spin or charge noise, reduces single-qubit coherence, in particular during wait and idle times in the algorithms. In addition, charge noise affects the coupling strength J during the implementation of the C*Z* gates. Numerical simulations (solid lines in Fig. 3c, d and Extended Data Fig. 10) show that quasi-static nuclear-spin and charge noise can reproduce most of the features seen in the data for the two-qubit algorithm (Methods). Smaller error contributions include residual coupling during single-qubit operations and miscalibrations.

Substantial improvements could be made in the performance of the processor by using isotopically purified ^{28}Si (refs 18, 19, 21), which would increase the coherence times of the qubits. Furthermore, recent experiments have shown that symmetrically operating an exchange gate by pulsing the tunnel coupling rather than the detuning leads to a gate that is less sensitive to charge noise, greatly improving fidelities[32,33]. With these improvements, and combined with more reproducible and scalable device structures, quantum computers with multiple qubits and fidelities above the fault-tolerance threshold should be realizable.

Online Content Methods, along with any additional Extended Data display items and Source Data, are available in the online version of the paper; references unique to these sections appear only in the online paper.

Received 14 August 2017; accepted 16 January 2018.
Published online 14 February 2018.

1. Barends, R. *et al.* Superconducting quantum circuits at the surface code threshold for fault tolerance. *Nature* **508,** 500–503 (2014).
2. Debnath, S. *et al.* Demonstration of a small programmable quantum computer with atomic qubits. *Nature* **536,** 63–66 (2016).
3. Loss, D. & DiVincenzo, D. P. Quantum computation with quantum dots. *Phys. Rev. A* **57,** 120–126 (1998).
4. Maurand, R. *et al.* A CMOS silicon spin qubit. *Nat. Commun.* **7,** 13575 (2016).
5. Vandersypen, L. M. K. *et al.* Interfacing spin qubits in quantum dots and donors—hot, dense, and coherent. *npj Quantum Inf.* **3,** 34 (2017).
6. Shulman, M. D. *et al.* Demonstration of entanglement of electrostatically coupled singlet-triplet qubits. *Science* **336,** 202–205 (2012).
7. Kim, D. *et al.* Quantum control and process tomography of a semiconductor quantum dot hybrid qubit. *Nature* **511,** 70–74 (2014).
8. Veldhorst, M. *et al.* A two-qubit logic gate in silicon. *Nature* **526,** 410–414 (2015).
9. Medford, J. *et al.* Self-consistent measurement and state tomography of an exchange-only spin qubit. *Nat. Nanotechnol.* **8,** 654–659 (2013).
10. Vandersypen, L. M. K. *et al.* Experimental realization of Shor's quantum factoring algorithm using nuclear magnetic resonance. *Nature* **414,** 883–887 (2001).
11. DiCarlo, L. *et al.* Demonstration of two-qubit algorithms with a superconducting quantum processor. *Nature* **460,** 240–244 (2009).
12. Gulde, S. *et al.* Implementation of the Deutsch–Jozsa algorithm on an ion-trap quantum computer. *Nature* **421,** 48–50 (2003).
13. van der Sar, T. *et al.* Decoherence-protected quantum gates for a hybrid solid-state spin register. *Nature* **484,** 82–86 (2012).

14. Bluhm, H. *et al.* Dephasing time of GaAs electron-spin qubits coupled to a nuclear bath exceeding 200 μs. *Nat. Phys.* **7,** 109–113 (2011).
15. Petta, J. R. *et al.* Coherent manipulation of coupled electron spins in semiconductor quantum dots. *Science* **309,** 2180–2184 (2005).
16. Zwanenburg, F. A. *et al.* Silicon quantum electronics. *Rev. Mod. Phys.* **85,** 961–1019 (2013).
17. Tyryshkin, A. M. *et al.* Electron spin coherence exceeding seconds in high-purity silicon. *Nat. Mater.* **11,** 143–147 (2012).
18. Veldhorst, M. *et al.* An addressable quantum dot qubit with fault-tolerant control-fidelity. *Nat. Nanotechnol.* **9,** 981–985 (2014).
19. Muhonen, J. T. *et al.* Storing quantum information for 30 seconds in a nanoelectronic device. *Nat. Nanotechnol.* **9,** 986–991 (2014).
20. Kawakami, E. *et al.* Gate fidelity and coherence of an electron spin in an Si/SiGe quantum dot with micromagnet. *Proc. Natl Acad. Sci. USA* **113,** 11738–11743 (2016).
21. Yoneda, J. *et al.* A quantum-dot spin qubit with coherence limited by charge noise and fidelity higher than 99.9%. *Nat. Nanotechnol.* **13,** 102–106 (2018).
22. Kawakami, E. *et al.* Electrical control of a long-lived spin qubit in a Si/SiGe quantum dot. *Nat. Nanotechnol.* **9,** 666–670 (2014).
23. Elzerman, J. M. *et al.* Single-shot read-out of an individual electron spin in a quantum dot. *Nature* **430,** 431–435 (2004).
24. Srinivasa, V., Nowack, K. C., Shafiei, M., Vandersypen, L. M. K. & Taylor, J. M. Simultaneous spin-charge relaxation in double quantum dots. *Phys. Rev. Lett.* **110,** 196803 (2013).
25. Pioro-Ladrière, M. *et al.* Electrically driven single-electron spin resonance in a slanting Zeeman field. *Nat. Phys.* **4,** 776–779 (2008).
26. Knill, E. *et al.* Randomized benchmarking of quantum gates. *Phys. Rev. A* **77,** 012307 (2008).
27. Fowler, A. G., Mariantoni, M., Martinis, J. M. & Cleland, A. N. Surface codes: towards practical large-scale quantum computation. *Phys. Rev. A* **86,** 032324 (2012).
28. Meunier, T., Calado, V. E. & Vandersypen, L. M. K. Efficient controlled-phase gate for single-spin qubits in quantum dots. *Phys. Rev. B* **83,** 121403 (2011).
29. Zajac, D. M. *et al.* Resonantly driven CNOT gate for electron spins. *Science* **359,** 439–442 (2018).
30. Deutsch, D. & Jozsa, R. Rapid solution of problems by quantum computation. *Proc. R. Soc. Lond. A* **439,** 553–558 (1992).
31. Grover, L. K. Quantum mechanics helps in searching for a needle in a haystack. *Phys. Rev. Lett.* **79,** 325–328 (1997).
32. Reed, M. D. *et al.* Reduced sensitivity to charge noise in semiconductor spin qubits via symmetric operation. *Phys. Rev. Lett.* **116,** 110402 (2016).
33. Martins, F. *et al.* Noise suppression using symmetric exchange gates in spin qubits. *Phys. Rev. Lett.* **116,** 116801 (2016).

Supplementary Information is available in the online version of the paper.

Acknowledgements This research was sponsored by the Army Research Office (ARO) under grant numbers W911NF-17-1-0274 and W911NF-12-1-0607. The views and conclusions contained in this document are those of the authors and should not be interpreted as representing the official policies, either expressed or implied, of the ARO or the US Government. The US Government is authorized to reproduce and distribute reprints for government purposes notwithstanding any copyright notation herein. Development and maintenance of the growth facilities used for fabricating samples is supported by DOE (DE-FG02-03ER46028). We acknowledge the use of facilities supported by NSF through the University of Wisconsin-Madison MRSEC (DMR-1121288). E.K. was supported by a fellowship from the Nakajima Foundation. We acknowledge financial support from the Marie Skłodowska-Curie actions—Nanoscale solid-state spin systems in emerging quantum technologies—Spin-NANO, grant agreement number 676108. We acknowledge discussions with S. Dobrovitski, C. Dickel, A. Rol, J. P. Dehollain, Z. Ramlakhan and members of the Vandersypen group, and technical assistance from R. Schouten, R. Vermeulen, M. Tiggelman, M. Ammerlaan, J. Haanstra, R. Roeleveld and O. Benningshof.

Author Contributions T.F.W. performed the experiment with help from E.K. and P.S., T.F.W. and S.G.J.P. analysed the data, S.G.J.P. performed the simulations of the algorithms, T.F.W., S.G.J.P., E.K., P.S., M.V., M.F., S.N.C., M.A.E. and L.M.K.V. contributed to the interpretation of the data and commented on the manuscript, D.R.W. fabricated the device, D.E.S. and M.G.L. grew the Si/SiGe heterostructure, T.F.W. wrote the manuscript (S.G.J.P. wrote parts of Methods) and L.M.K.V. conceived and supervised the project.

Author Information Reprints and permissions information is available at www.nature.com/reprints. The authors declare no competing financial interests. Readers are welcome to comment on the online version of the paper. Publisher's note: Springer Nature remains neutral with regard to jurisdictional claims in published maps and institutional affiliations. Correspondence and requests for materials should be addressed to L.M.K.V. (l.m.k.vandersypen@tudelft.nl).

Reviewer Information *Nature* thanks H. Bluhm and the other anonymous reviewer(s) for their contribution to the peer review of this work.

METHODS

Estimate of initialization and readout errors for Q1 and Q2. The initialization and readout procedures for Q1 and Q2 are described in Extended Data Fig. 2. The initialization and readout fidelities of Q2 were extracted by performing the following three experiments and measuring the resulting spin-up probabilities (P_1, P_2 and P_3): (i) initialize Q2 and wait for $7T_1$; (ii) initialize Q2; and (iii) initialize and perform a π rotation on Q2. These three spin-up probabilities are related to the initialization fidelity (γ_2) and the spin-up and spin-down readout fidelities ($F_{|0\rangle,2}$ and $F_{|1\rangle,2}$) by

$$\begin{aligned} P_1 &= 1 - F_{|0\rangle,2} \\ P_2 &= F_{|1\rangle,2}(1-\gamma_2) + (1-F_{|0\rangle,2})\gamma_2 \\ \frac{P_3}{P_{\pi 2}} &= F_{|1\rangle,2}\gamma_2 + (1-F_{|0\rangle,2})(1-\gamma_2) \end{aligned} \tag{2}$$

where $P_{\pi 2}$ is the expected probability to be in the spin-up state after the application of the π pulse for Q2, which is determined as described below. In equation (2) we assume that a waiting time of $7T_1$ leads to 100% initialization and that the measured spin-up counts are due to the readout infidelity. By solving these equations we can extract the initialization and readout fidelities. For Q1, we performed initialization by pulsing to a spin-relaxation hotspot (Extended Data Fig. 5) for $500T_1$ and we therefore assume that the initialization fidelity is about 100%. Consequently, the readout fidelities of Q1 were extracted by performing only experiments (ii) and (iii) above. The readout and initialization fidelities for Q1 (Q2) during the state tomography experiments were estimated to be $\gamma_1 > 99\%$ ($\gamma_2 > 99\%$), $F_{|0\rangle,1} = 92\%$ ($F_{|0\rangle,2} = 86\%$) and $F_{|1\rangle,1} = 54\%$ ($F_{|1\rangle,2} = 76\%$), for which we used $P_{\pi 1} = 98\%$ ($P_{\pi 2} = 97\%$) on the basis of simulations that include the dephasing time of the qubits (see below). The average measurement fidelity $F_m = (F_{|0\rangle} + F_{|1\rangle})/2$ for Q1 (Q2) is 73% (81%). These fidelities are limited mostly by the finite electron temperature $T_e \approx 130$ mK and the fast spin-relaxation time of Q2 ($T_1 = 3.7$ ms), which is probably caused by a spin-relaxation hotspot that is due to a similar valley splitting and Zeeman energy[36].

Removing readout errors from the measured two-spin probabilities. In the experiment the measured two-spin probabilities $\boldsymbol{P}^{\mathrm{M}} = (P^{\mathrm{M}}_{|00\rangle}, P^{\mathrm{M}}_{|01\rangle}, P^{\mathrm{M}}_{|10\rangle}, P^{\mathrm{M}}_{|11\rangle})^{\mathrm{T}}$ include errors due to the limited readout fidelities $F_{|0\rangle,i}$ and $F_{|1\rangle,i}$ of spin-down (0) and spin-up (1) electrons for qubit i. To remove these readout errors and obtain the actual two-spin probabilities $\boldsymbol{P} = (P_{|00\rangle}, P_{|01\rangle}, P_{|10\rangle}, P_{|11\rangle})^{\mathrm{T}}$, we use the relationship $\boldsymbol{P}^{\mathrm{M}} = (\hat{F}_1 \otimes \hat{F}_2)\boldsymbol{P}$, where

$$\hat{F}_i = \begin{pmatrix} F_{|0\rangle,i} & 1-F_{|1\rangle,i} \\ 1-F_{|0\rangle,i} & F_{|1\rangle,i} \end{pmatrix} \tag{3}$$

State tomography. The density matrix of a two-qubit state can be expressed as $\rho = \sum_{i=1}^{16} c_i M_i$, where M_i are 16 linearly independent measurement operators. The coefficients c_i are calculated from the expectation values m_i of the measurement operators using a maximum-likelihood estimate[11,37]. The expectation values were calculated by performing 16 combinations of (I, X, Y, X^2) pre-rotations on Q1 and Q2 and measuring the two-spin probabilities over 10,000 repetitions per measurement. The two-spin probabilities were converted to actual two-spin probabilities by removing the readout errors using equation (3). To calculate the density matrices shown in Fig. 2 we used only the data from the (I, X, Y) pre-rotations on the assumption that I will give a more accurate estimate of the expectation values than X^2 owing to gate infidelities. If we include X^2 then we achieve state fidelities of 80%–84% and concurrences of 67%–71% (Supplementary Information, section S3). In the analysis we assume that the pre-rotations are perfect, which is a reasonable approximation owing to the high single-qubit Clifford-gate fidelities (98%) compared to the measured state fidelities (85%–89%). The state tomography experiment was performed in parallel with the fidelity experiments described above and a Ramsey experiment that was used to calibrate the frequency actively.

Error analysis. Error analysis was performed using a Monte Carlo method by assuming a multinomial distribution for the measured two-spin probabilities and a binomial distribution for the probabilities P_1, P_2 and P_3 used to calculated the fidelities. Values from these distributions were sampled randomly and the procedures outlined above were followed. This was repeated 250 times to build up the final distributions that we used to determine the mean values and the standard deviation.

Simulation of two electron spins in a double quantum dot. In the simulation, we consider two electrons in two tunnel-coupled quantum dots, with an external magnetic field B_0 applied to both dots. In addition to this field, the two dots have different Zeeman energies owing to the magnetic-field gradient across the double quantum dot that is generated by the micromagnets. The Zeeman energy of Q1 (Q2) is denoted as E_{Z1} (E_{Z2}). The double-quantum-dot system is modelled by the Hamiltonian[38]

$$\hat{H} = \begin{pmatrix} -\beta & 0 & 0 & 0 & 0 & 0 \\ 0 & -\Delta v & 0 & 0 & t & t \\ 0 & 0 & \Delta v & 0 & -t & -t \\ 0 & 0 & 0 & \beta & 0 & 0 \\ 0 & t & -t & 0 & U_1+\varepsilon & 0 \\ 0 & t & -t & 0 & 0 & U_2-\varepsilon \end{pmatrix}$$

with the states $|00\rangle$, $|01\rangle$, $|10\rangle$, $|11\rangle$, S(2, 0) and S(0, 2) as the eigenbasis. In this Hamiltonian, $\beta = (E_{Z1} + E_{Z2})/2$, $\Delta v = (E_{Z1} - E_{Z2})/2$, $\sqrt{2}t$ is the tunnel coupling between the (1, 1) and (0, 2)/(2, 0) singlet states, and U_i is the on-site charging energy of the ith quantum dot. To study the phases of the qubits during the control pulses, the Hamiltonian is transformed into a rotating frame using

$$\widetilde{H} = VHV^{\dagger} + i\hbar(\partial_t V)V^{\dagger} \tag{4}$$

where $V = \exp\{-i[E_{Z1}(\hat{\sigma}_z \otimes \hat{I}) + E_{Z2}(\hat{I} \otimes \hat{\sigma}_z)]t\}$ is the matrix that describes the unitary transformation normalized such that $\hbar = 1$. The transformed Hamiltonian is

$$\widetilde{H} = \begin{pmatrix} 0 & 0 & 0 & 0 & 0 & 0 \\ 0 & 0 & 0 & 0 & te^{i\Delta vt} & te^{i\Delta vt} \\ 0 & 0 & 0 & 0 & -te^{-i\Delta vt} & -te^{-i\Delta vt} \\ 0 & 0 & 0 & 0 & 0 & 0 \\ 0 & te^{-i\Delta vt} & -te^{i\Delta vt} & 0 & U_1+\varepsilon & 0 \\ 0 & te^{-i\Delta vt} & -te^{i\Delta vt} & 0 & 0 & U_2-\varepsilon \end{pmatrix}$$

To model the single-qubit gates during EDSR, we use the Hamiltonian

$$\hat{H}_{\mathrm{MW}} = \sum_k B_{\mathrm{MW},k} \cos(\omega_k t + \phi_k)(\hat{\sigma}_x \otimes \hat{I} + \hat{I} \otimes \hat{\sigma}_x)$$

which assumes the same drive amplitude on each of the qubits. Here, k represents the kth signal, which has an angular frequency ω_k, phase φ_k and driving amplitude $B_{\mathrm{MW},k}$. This Hamiltonian is transformed into the rotating frame using equation (4), and the rotating-wave approximation can be made to remove the fast-driving elements because the Rabi frequency is much smaller than the Larmor precession. Doing so gives the Hamiltonian

$$\widetilde{H}_{\mathrm{MW}} = \sum_k \begin{pmatrix} 0 & \Omega_k e^{i\Delta\omega_1 t} & \Omega_k e^{i\Delta\omega_2 t} & 0 & 0 & 0 \\ \Omega_k^* e^{-i\Delta\omega_1 t} & 0 & 0 & \Omega_k e^{i\Delta\omega_2 t} & 0 & 0 \\ \Omega_k^* e^{-i\Delta\omega_2 t} & 0 & 0 & \Omega_k e^{i\Delta\omega_1 t} & 0 & 0 \\ 0 & \Omega_k^* e^{-i\Delta\omega_2 t} & \Omega_k^* e^{-i\Delta\omega_1 t} & 0 & 0 & 0 \\ 0 & 0 & 0 & 0 & 0 & 0 \\ 0 & 0 & 0 & 0 & 0 & 0 \end{pmatrix}$$

where $\Omega_k = B_{\mathrm{MW},k} e^{i\phi_k}$, Ω_k^* is the complex conjugate of Ω_k and $\Delta\omega_k = \omega_k - \omega_{\mathrm{qubit}_i}$.

The dynamics of the two-qubit system can be described by the Schrödinger–von Neumann equation, $\rho_{t+\Delta t} = e^{-i\widetilde{H}t/\hbar}\rho_t e^{i\widetilde{H}t/\hbar}$, which we solved numerically using the Armadillo linear algebra library in C++, with the matrix exponentials solved using scaling methods ($e^A = \prod_s e^{A/2^s}$) and a Taylor expansion. In the experiments, we apply microwave pulses with square envelopes that have a finite rise time owing to the limited bandwidth of the in-phase (I) and quadrature (Q) modulation channels of the microwave vector source. For simplicity, we approximate these microwave pulses with a perfect square envelope. The detuning pulses were modelled with a finite rise and fall time using a Fermi–Dirac function to take (a)diabatic effects into account. The finite rise time was set to 2 ns on the basis of the cut-off frequency of the low-pass filter that was attached to the lines and used to pulse the detuning pulses.

Modelling noise in the simulation. In the model we include three different noise sources. The first two noise sources are from fluctuating nuclear spins in the natural silicon quantum well, which generate quasi-static magnetic noise that couples to the qubits via the $Z \otimes I$ and $I \otimes Z$ terms in the Hamiltonian. These fluctuations are treated as two independent noise sources because D1 and D2 are in different locations in the quantum well and sample the field from different nuclear spins. The third noise source is charge noise, which can couple to the qubits via the magnetic-field gradient from the micromagnets. We model this noise as magnetic noise on the $Z \otimes I$ and $I \otimes Z$ terms in the Hamiltonian. Charge noise also couples to the spins via the exchange coupling, which leads to noise on the $Z \otimes Z$ term in the Hamiltonian.

In our simulations, we treat these noise sources as quasi-static, whereby the noise is static within each cycle and changes only between measurement cycles. This approximation is reasonable because the noise in the system is pink, with

low frequencies in the power spectrum being more pronounced[20]. The static noise due to each noise source was modelled by sampling a random value from a Gaussian distribution with standard deviation σ, corresponding to the contribution to dephasing of that noise process. After sampling the static noise, the time evolution of the qubits during a gate sequence was calculated. This time evolution was averaged over many repetitions to give the final result; for each repetition new values for the static noise were sampled. In total, for each simulation we performed 5,000 repetitions to ensure convergence.

In the experiment, single-qubit gates are performed at higher detuning near the centre of the (1, 1) charge region at a detuning of $\varepsilon = -3$ meV, where the exchange is low ($J_{\mathrm{off}} = 270$ kHz); a two-qubit CZ gate is performed by pulsing to low detuning $\varepsilon = -0.7$ meV, where the exchange is high ($J_{\mathrm{on}} = 6$ MHz). To estimate the relative effect of charge noise on the $Z \otimes I$, $I \otimes Z$ and $Z \otimes Z$ terms at these two detuning points, we use the spectroscopy data for the qubits as a function of detuning energy shown in Extended Data Fig. 8. The four resonances observed correspond to the four transitions shown in Extended Data Fig. 8c between the $|00\rangle$, $|01\rangle$, $|10\rangle$ and $|11\rangle$ eigenstates. From fits of this data we estimate the derivative of the transition energy from state $|i\rangle$ to $|j\rangle$ at a particular detuning, $\mathrm{d}E_{|i\rangle\rightarrow|j\rangle}/\mathrm{d}\varepsilon|_{\varepsilon}$, which is directly proportional to the magnitude of fluctuations in the transition energy under the influence of charge noise. Fixing the energy of the $|00\rangle$ state, from these derivatives we calculate the relative noise levels on the other energy eigenstates:

$$B(\varepsilon) = \begin{pmatrix} 0 \\ \left.\dfrac{\partial E_{|00\rangle\leftrightarrow|01\rangle}}{\partial \varepsilon}\right|_{\varepsilon} \\ \left.\dfrac{\partial E_{|00\rangle\leftrightarrow|10\rangle}}{\partial \varepsilon}\right|_{\varepsilon} \\ \left.\dfrac{\partial E_{|00\rangle\leftrightarrow|01\rangle}}{\partial \varepsilon}\right|_{\varepsilon} + \left.\dfrac{\partial E_{|01\rangle\leftrightarrow|11\rangle}}{\partial \varepsilon}\right|_{\varepsilon} \end{pmatrix} \quad (5)$$

In the regime in which $J \ll \Delta v$, the Hamiltonian of the system can be approximated as $H = -E_{Z1}(Z \otimes I) - E_{Z2}(I \otimes Z) + J(Z \otimes Z) - J/4(I \otimes I)$. The relative noise on E_{Z1}, E_{Z2} and J is found by decomposing the four noise levels in equation (5) in terms of the basis $(-Z \otimes I, -I \otimes Z, Z \otimes Z, -I \otimes I/4)$ by calculating $A^{-1}B(\varepsilon)$, where

$$A = \begin{pmatrix} -1/2 & -1/2 & 1/4 & -1/4 \\ -1/2 & 1/2 & -1/4 & -1/4 \\ 1/2 & -1/2 & -1/4 & -1/4 \\ 1/2 & 1/2 & 1/4 & -1/4 \end{pmatrix}$$

We estimate the relative composition of the noise for (E_{Z1}, E_{Z2}, J) at $\varepsilon = -3$ meV to be (0.12, 0.24, 0) and at $\varepsilon = -0.7$ meV ($J = 6$ MHz) to be (0.61, 0.23, 0.26). Note that this is a crude approximation because we take into account only voltage noise along the detuning axis, whereas in reality charge noise acts also along other axes. We do not include calibration errors in the simulation. On the basis of the AllXY and Ramsey calibration experiments (Supplementary Information, section S2), miscalibrations of a few per cent are possible.

Estimating charge noise from the decay of the decoupled CZ oscillations. The dephasing due to charge noise coupling into the double-quantum-dot system via the exchange energy is measured by varying the duration of the DCZ gate between two $\pi/2$ pulses on Q1 (Extended Data Fig. 9) for $J = 6$ MHz. The DCZ gate removes the effect of quasi-static noise on the $Z \otimes I$ and $I \otimes Z$ terms in the Hamiltonian, and the decay time of the oscillations $T_2 = 1{,}640$ ns is assumed to be due to noise on the $Z \otimes Z$ term. The data are fitted using either a Gaussian (black line) or exponential decay (red line). The exponential decay seems to fit better to the data, which suggests that either higher-frequency noise plays a part[39] or the origin of the noise is from a few two-level fluctuators[40]. Because the decay time of the DCZ gate is longer than that of the CZ gate, there is also a substantial quasi-static noise contribution.

For simplicity, we include only the quasi-static contribution in our noise model. For Gaussian quasi-static noise with standard deviation σ_{ε}, the decay time is

$$1/T_2 = \frac{1}{2}\left.\frac{\partial J}{\partial \varepsilon}\right|_{\varepsilon} \frac{\sigma_{\varepsilon}}{\sqrt{2}\hbar}$$

The factor of 1/2 is needed because it is the noise on $J/2$ that contributes to the decay. This is because the target qubit precesses with a frequency of $J/2$ (ignoring the $I \otimes Z$ and $Z \otimes I$ terms) when the control qubit is in an eigenstate. From the dephasing time and $\mathrm{d}J/\mathrm{d}\varepsilon|_{\varepsilon} = 1.0 \times 10^{-4}$ extracted from Extended Data Fig. 8a, b, we estimate the charge noise on the detuning to be 11 μeV. The data in Extended Data Fig. 9 used to extract this value were collected over about 40 min with no active calibration on the detuning pulse. The time needed for each single-shot measurement was around 10 ms.

Simulations of the two-qubit algorithms. To describe the double-quantum-dot system used in the experiment, we use the following parameters in the Hamiltonian. The qubit frequencies were chosen to be $E_{Z1}/h = 18.4$ GHz and $E_{Z2}/h = 19.7$ GHz, and the on-site charging energies to be $U_1 = U_2 = 3.5$ meV, comparable to the experimental values. The tunnel coupling was chosen to be $t = 210$ MHz so that the residual exchange energy J_{off} was 300 kHz, similar to that measured in the experiment. The two-qubit gates were implemented by choosing a value of ε for which $J = 6$ MHz when diagonalizing the Hamiltonian $\hat{H}$.

The results of the simulations for the Deutsch–Josza algorithm and the Grover algorithm using the CZ gate and the DCZ gate are shown in Fig. 3 and Extended Data Fig. 10. The amplitudes for the three noise sources used in the simulations were identical for all 16 panels. The value of charge noise used was 11 μeV (see above), whereas the nuclear-spin noise for Q1 and Q2 was chosen to give the single-qubit decoherence times $T_2^* = 1{,}000$ ns and $T_2^* = 600$ ns measured in the Ramsey experiment (Extended Data Fig. 3). This gave a dephasing time of Q1 (Q2) due to nuclear spin of $T_{2\mathrm{nuc}}^* = 1{,}200$ ns ($T_{2\mathrm{nuc}}^* = 800$ ns). The simulations reproduce many of the features of the experimental data for the algorithms.

By simulating the algorithms, we learn that the residual exchange coupling J_{off} during single-qubit gates has little effect (less than 2%) on the result of the algorithms. Furthermore, we find that without noise on the single-qubit terms it is difficult to get consistent agreement with the data. Additional noise on the coupling strength improves the agreement. In contrast to the cases of the Deutsch–Jozsa algorithm and the conventional Grover algorithm, the simulation for the decoupled version of Grover's algorithm predicts a better outcome than the experiment. This case uses the longest sequence of operations, leaving the most room for discrepancies between model and experiment to build up. These discrepancies could have several origins: (i) the implementation of the static noise model not being accurate enough; (ii) non-static noise having a role; (iii) the calibration errors in the gates that were left out of the simulation; or (iv) variations in the qubit parameters and noise levels between experiments. Finally, we note that initialization and readout errors are not taken into account in the simulations. Because initialization errors are negligible and the data shown were renormalized to remove the effect of readout errors, the simulated and experimental results can be compared directly.

Data availability. The raw data and analysis that support the findings of this study are available in the Zenodo repository (https://doi.org/10.5281/zenodo.1135014).

36. Yang, C. H. *et al.* Spin-valley lifetimes in a silicon quantum dot with tunable valley splitting. *Nat. Commun.* **4,** 2069 (2013).
37. James, D. F. V., Kwiat, P. G., Munro, W. J. & White, A. G. Measurement of qubits. *Phys. Rev. A* **64,** 052312 (2001).
38. Das Sarma, S., Wang, X. & Yang, S. Hubbard model description of silicon spin qubits: charge stability diagram and tunnel coupling in Si double quantum dots. *Phys. Rev. B* **83,** 235314 (2011).
39. Dial, O. E. *et al.* Charge noise spectroscopy using coherent exchange oscillations in a singlet-triplet qubit. *Phys. Rev. Lett.* **110,** 146804 (2013).
40. Ithier, G. *et al.* Decoherence in a superconducting quantum bit circuit. *Phys. Rev. B* **72,** 134519 (2005).

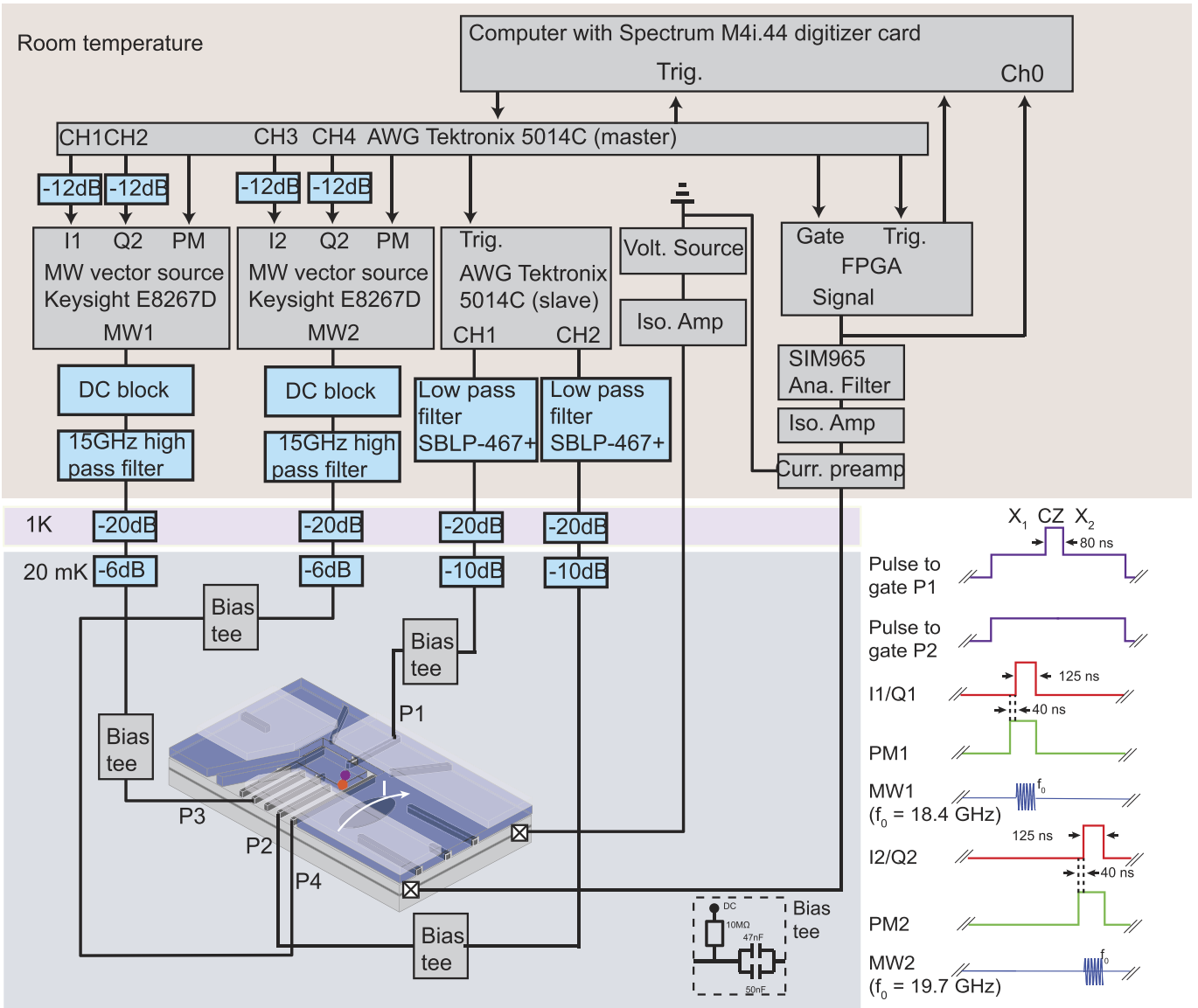

Extended Data Figure 1 | Schematic of the measurement set-up. The sample was bonded to a printed circuit board (PCB) mounted onto the mixing chamber of a dilution refrigerator. All measurements were performed at the base temperature of the fridge, $T_{base} \approx 20$ mK. DC voltages were applied to all of the gate electrodes using room-temperature digital-to-analogue converters via filtered lines (not shown). Voltage pulses were applied to plunger gates P1 and P2 using a Tektronix 5014C arbitrary waveform generator (AWG) with 1-GHz clock rate. The signals from the AWGs passed through a room-temperature low-pass filter and attenuators at different stages of the fridge and were added to the DC signals via bias tees mounted on the PCB. Two Keysight E8267D vector microwave sources, MW1 and MW2, were used to apply microwaves (18–20 GHz) to perform EDSR on Q1 and Q2, respectively. The signals passed through room-temperature DC blocks and custom-built 15-GHz high-pass filters and attenuators at different stages of the fridge and were added to the DC signals via bias tees mounted on the PCB. The output of the microwave source (phase, frequency, amplitude and duration) was controlled with I/Q vector modulation. The I/Q signals were generated with another Tektronix 5041C, which was the master device for the entire set-up and provided trigger signals for the other devices. In addition to the vector modulation, we used pulse modulation to give an on/off microwave power output ratio of 120 dB. Although I/Q modulation can be used to output multiple frequencies, the bandwidth of the AWG was not sufficient to control both qubits with one microwave source owing to their large separation in frequency (1.3 GHz). The sensor current I was converted to a voltage signal with a custom-built preamplifier, and an isolation amplifier was used to separate the signal ground, with the measurement equipment grounded to reduce interference. Following this, a 20-kHz Bessel low-pass filter was applied to the signal using a SIM965 analogue filter. A field-programmable gate array (FPGA) analysed the voltage signal during the readout and assigned the trace to be spin-up if the voltage fell below a certain threshold. The voltage signal could also be measured with a digitizer card in the computer. The shapes of the pulses generated by the AWGs and microwave sources during qubit manipulation, along with the typical timescales, are shown in the lower right. Square pulses were used to perform the CZ gate and as the input for the I/Q modulation to generate microwave pulses. The pulse modulation was turned on 40 ns before turning on the I/Q signal, owing to the time needed for the modulation to switch on.

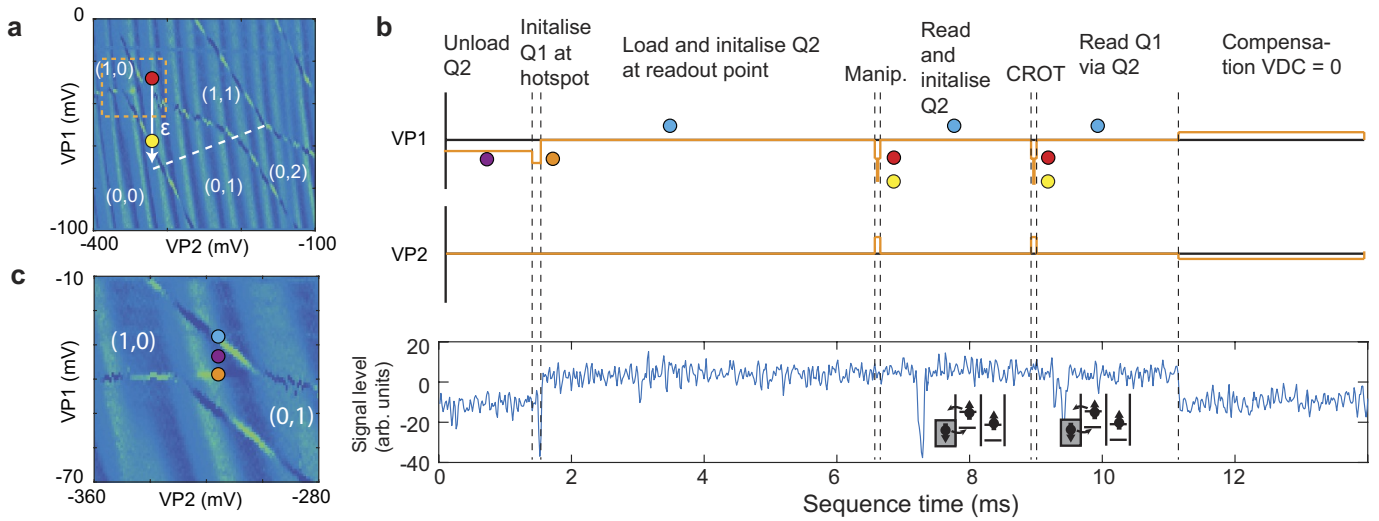

Extended Data Figure 2 | Measurement protocol for two electron spins. **a**, Stability diagram of the double quantum dot, showing the positions in gate space used to perform single-qubit gates (red circle) and two-qubit gates (yellow circle). The map shows the numerically obtained differential current dI/dV_{P1} through the quantum-dot charge sensor as a function of the voltages on P1 and P2. The white dashed line is the (1, 1)–(0,2) inter-dot transition line. The white arrow indicates the detuning axis ε used in the experiments. Although the detuning pulse for the two-qubit gate crosses the charge-addition lines of D1 and D2, the quantum dots remain in the (1, 1) charge state because the pulse time is much shorter than the electron tunnel times to the reservoirs. **b**, Plot of the voltage pulses applied to plunger gates P1 and P2 and the response of the quantum-dot charge sensor over one measurement cycle. D2 is unloaded by pulsing into the (1, 0) charge region for 1.5 ms (purple circle). The electron on D1 is initialized to spin-down by pulsing to a spin-relaxation hotspot at the (1, 0) and (0, 1) charge degeneracies (orange circle) for 50 μs (see Extended Data Fig. 5). D2 is loaded with a spin-down electron by pulsing to the readout position for 4 ms (blue circle). During manipulation, the voltages on the plunger gates are pulsed to the red circle for single-qubit gates and to the yellow circle for two-qubit gates, where the exchange is about 6 MHz. After manipulation, the spin of the electron on D2 is measured by pulsing to the readout position (blue circle) for 0.7 ms, where the Fermi level of the reservoir is between the spin-up and spin-down electrochemical potentials of D2. If the electron is spin-up then it can tunnel out, after which a spin-down electron tunnels back in. These two tunnel events are detected by the quantum-dot sensor as a single blip in the current signal. An additional 1.3 ms is spent at the readout position so that D2 is initialized to spin-down with high fidelity. Following this, Q1 is measured by first performing a CROT gate at the yellow circle so that $\alpha|00\rangle + \beta|10\rangle \xrightarrow{\text{CROT12}} \alpha|00\rangle + \beta|11\rangle$, where CROT12 indicates a CROT gate with Q1 as the control and Q2 as the target. A projective measurement of Q1 is then performed by measuring Q2 at the readout position for 0.7 ms (blue circle). Finally, we add a compensation pulse to VP1 and VP2 so that over the measurement cycle $V_{DC} = 0$ to mitigate charging effects in the bias tees. **c**, Close-up of the stability diagram in **a** showing the positions in gate space used for initialization and readout.

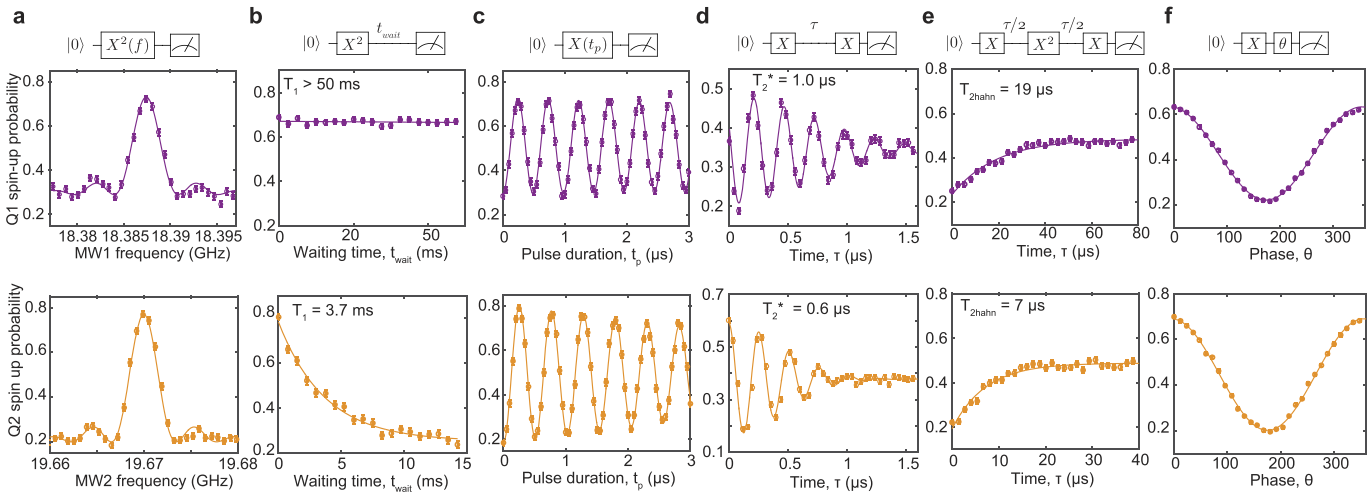

Extended Data Figure 3 | Single-qubit properties and two-axis control. The purple (top) and orange (bottom) data points correspond to measurements performed on Q1 and Q2, respectively, in the (1, 1) regime (red circle in Extended Data Fig. 2). **a**, Spin-up fraction as a function of the microwave frequency of an applied π pulse, showing a resonant frequency of 18.387 GHz (19.670 GHz) for Q1 (Q2). **b**, The spin-relaxation time is measured by preparing the qubit to spin-up and varying the wait time before readout. From the exponential decay in the spin-up probability we measure $T_1 > 50$ ms ($T_1 = 3.7 \pm 0.5$ ms) for Q1 (Q2). **c**, Spin-up probability as a function of microwave duration, showing Rabi oscillations of 2.0 MHz for Q1 and Q2. **d**, The dephasing time is measured by applying a Ramsey pulse sequence and varying the free evolution time τ. Oscillations were added artificially to improve the fit of the decay by making the phase of the last microwave pulse dependent on the free evolution time, $\phi = \sin(\omega\tau)$, where $\omega = 4$ MHz. By fitting the data with a Gaussian decay, $P_{|1\rangle} \propto \exp[-(\tau/T_2^*)^2]\sin(\omega\tau)$, we extract $T_2^* = 1.0 \pm 0.1$ μs ($T_2^* = 0.6 \pm 0.1$ μs) for Q1 (Q2). In the measurement for Q1, the first π/2 microwave pulse is a Y gate. The Ramsey measurement was performed over about 20 min with the frequency calibrated every approximately 1 min. **e**, The coherence time of Q1 (Q2) can be extended to $T_{2\mathrm{Hahn}} = 19 \pm 3$ μs ($T_{2\mathrm{Hahn}} = 7 \pm 1$ μs) by a Hahn echo sequence. The coherence time is extracted from an exponential fit to the spin-up probability as a function of the free evolution time in the Hahn echo sequence. **f**, Full two-axis control is demonstrated by applying two π/2 pulses and varying the phase of the second one. All error bars are 1σ from the mean.

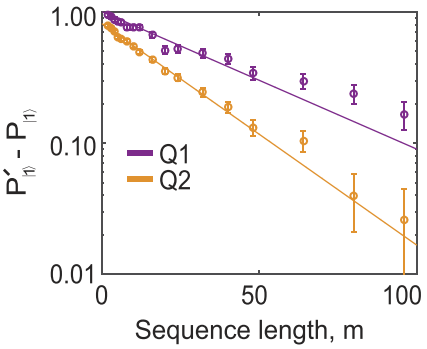

Extended Data Figure 4 | Randomized benchmarking of single-qubit gates. Randomized benchmarking of the single-qubit gates for each qubit is performed by applying a randomized sequence of a varying number of Clifford gates m to either the $|1\rangle$ or $|0\rangle$ state and measuring the final spin-up probability $P'_{|1\rangle}$ or $P_{|1\rangle}$, respectively. All gates in the Clifford group are decomposed into gates from the set $\{I, \pm X, \pm X^2, \pm Y, \pm Y^2\}$. The purple (orange) data points show the difference in the spin-up probabilities $P'_{|1\rangle} - P_{|1\rangle}$ for Q1 (Q2) as a function of sequence length. For each sequence length m we average over 32 different randomized sequences. From an exponential fit (solid lines) of the data, $P'_{|1\rangle} - P_{|1\rangle} = ap^m$, we estimate average Clifford-gate fidelities $F_C = 1 - (1 - p)/2$ of 98.8% and 98.0% for Q1 and Q2, respectively. The last three data points from both datasets were omitted from the fits because they deviate from a single exponential[20]. All error bars are 1σ from the mean.

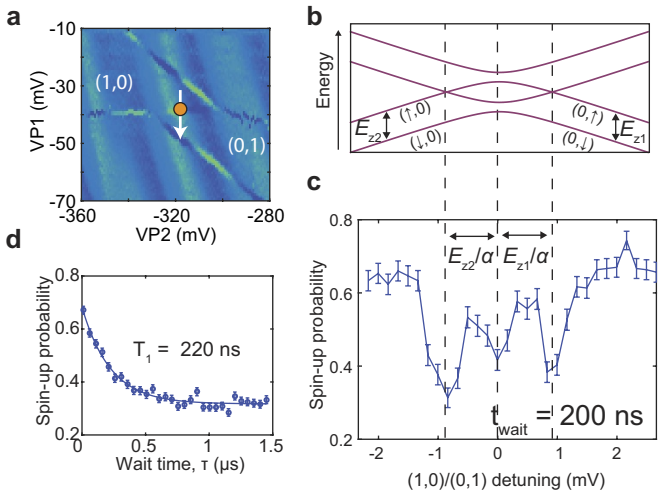

Extended Data Figure 5 | Spin-relaxation hotspots used for high-fidelity initialization. a, Close-up stability diagram of the (1, 0)–(0, 1) charge transition. The white arrow defines the detuning axis between D1 and D2 controlled with P1. **b**, Schematic of the energy-level diagram as a function of detuning for one electron spin in a double quantum dot. **c**, Spin-relaxation hotspots are measured by preparing the electron on D1 to spin-up using EDSR, applying a voltage pulse along the detuning axis (white arrow in **a**) for a wait time of 200 ns and performing readout of the electron spin. We observe three dips in the spin-up probability, which correspond to spin-relaxation hot spots. The first and third hotspot are due to anticrossings between the (0, ↓) and (↑, 0) states and the (↓, 0) and (0, ↑) states[24]. The second hotspot occurs at zero detuning. The voltage separation between the first and third hot spot corresponds to the sum of the Zeeman energy of D1 and D2 divided by the gate lever arm α along the detuning axis. Knowing precisely the Zeeman energies from EDSR spectroscopy, we can accurately extract the gate lever arm to be $\alpha = 0.09e$. **d**, The spin-relaxation time at zero detuning (orange circle in **a**) is found to be $T_1 = 220$ ns by measuring the exponential decay of the spin-up probability as a function of wait time τ at zero detuning. All error bars are 1σ from the mean.

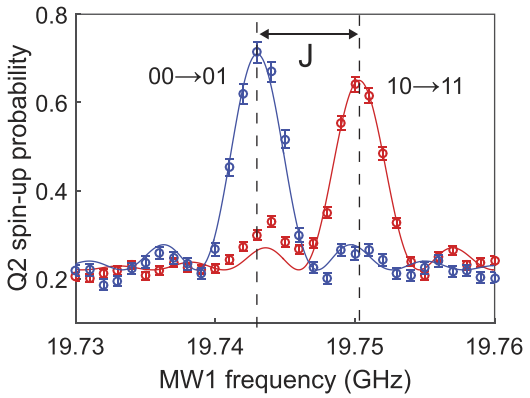

Extended Data Figure 6 | Two-qubit CROT gate. a, Microwave spectroscopy of Q2 close to zero detuning between the (1, 1) and (0, 2) states (yellow dot in Extended Data Fig. 2a) with the exchange coupling on. The blue and red curves show the resonance of Q2 after preparing Q1 into spin-down and spin-up, respectively. The resonance frequency of Q2 shifts by the exchange coupling, and by applying a π pulse at one of these frequencies we can perform a CROT gate, which is equivalent to a CNOT gate up to a $\hat{z}$ rotation. As discussed in the main text, this CROT gate is used to perform the projective measurement of Q1. All error bars are 1σ from the mean.

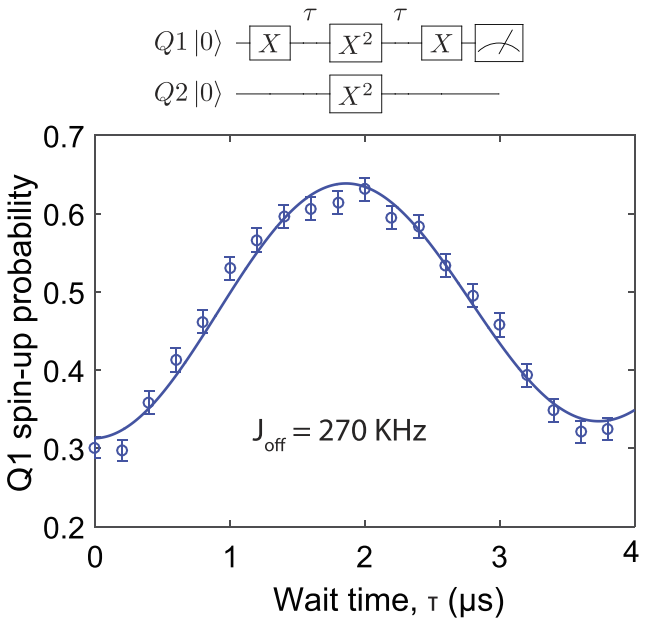

Extended Data Figure 7 | Measurement of J_{off} using a decoupling sequence. The exchange coupling J_{off} during single-qubit gates is measured using a two-qubit Hahn echo sequence, which cancels out any unconditional $\hat{z}$ rotations during the free evolution time τ. Fitting the spin-up probability as a function of free evolution time τ using the functional form $\sin(2\pi J_{off}\tau)$, we extract $J_{off} = 270$ kHz. All error bars are 1σ from the mean.

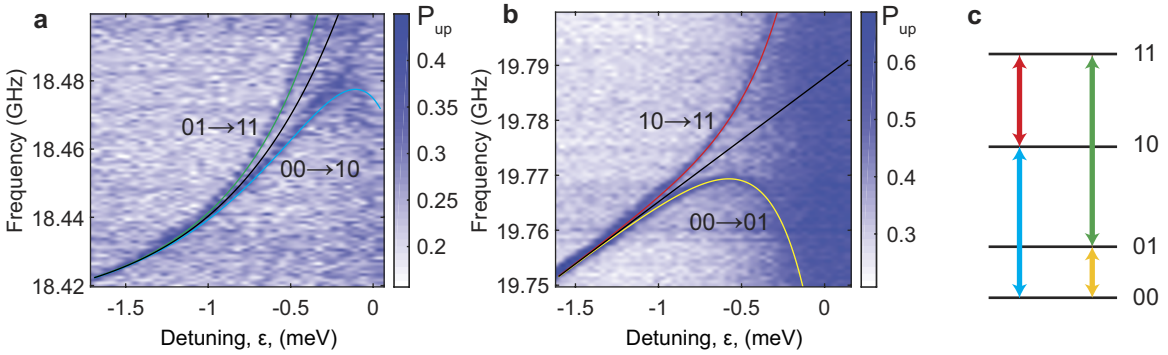

Extended Data Figure 8 | Microwave spectroscopy of Q1 and Q2. **a**, **b**, Spectroscopy of Q1 (**a**) and Q2 (**b**) versus detuning energy ε after initializing the other qubit to $(|0\rangle + |1\rangle)/\sqrt{2}$. Towards $\varepsilon = 0$ there are two resonances each for Q1 and Q2, which are separated by the exchange energy $J(\varepsilon)/h$. As discussed, the Zeeman energy $E_Z(\varepsilon)$ of Q1 and Q2 also depends on detuning because changes to the applied voltages shift the position of the electron in the magnetic-field gradient. The four resonance frequencies are fitted (green, blue, red and yellow lines) with $f_{jk} = E_{Zj}(\varepsilon) + (-1)^{k+1}J(\varepsilon)$, where j denotes the qubit and k denotes the state of the other qubit. The data are fitted well using $J(\varepsilon) \propto e^{c_1\varepsilon}$, $E_{Z1}(\varepsilon) \propto e^{c_2\varepsilon}$, and $E_{Z2}(\varepsilon) \propto \varepsilon$. The fitted Zeeman energies of Q1 and Q2 are shown by the black lines. We observe that the Zeeman energy of Q1 has an exponential dependence towards the (0, 2) charge regime ($\varepsilon = 0$). This observation can be explained by the electron delocalizing from D1 towards D2, which has a much higher Zeeman energy. **c**, Schematic of the colour-coded transitions that correspond to the resonances in **a** and **b**.

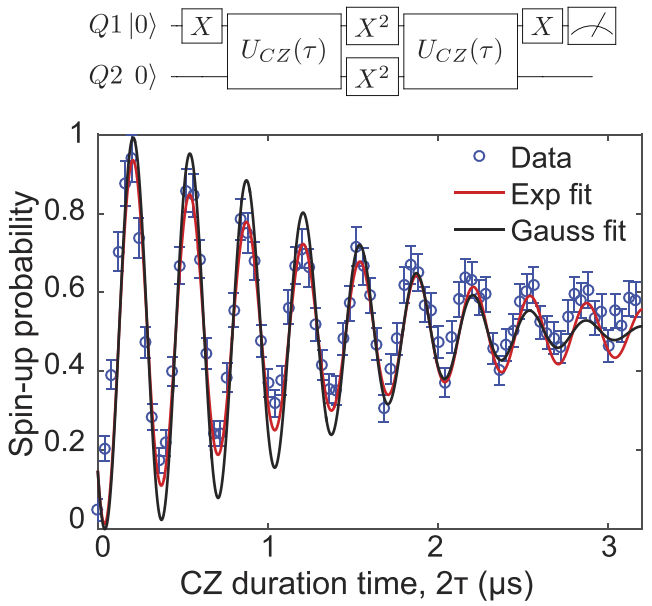

Extended Data Figure 9 | Decay of the decoupled CZ oscillations. The normalized spin-up probability of Q1 as a function of the total duration time 2τ of the two CZ gates in the DCZ sequence. The data are fitted using a sinusoid, $P_{|1\rangle} = 0.5\sin(2\pi J\tau) + 0.5$, with either a Gaussian (black line; $e^{-(2\tau/T_2)^2}$) or exponential (red line; $e^{-2\tau/T_2}$) decay. From these fits we find a decay time of $T_2 = 1.6\,\mu s$. All error bars are 1σ from the mean.

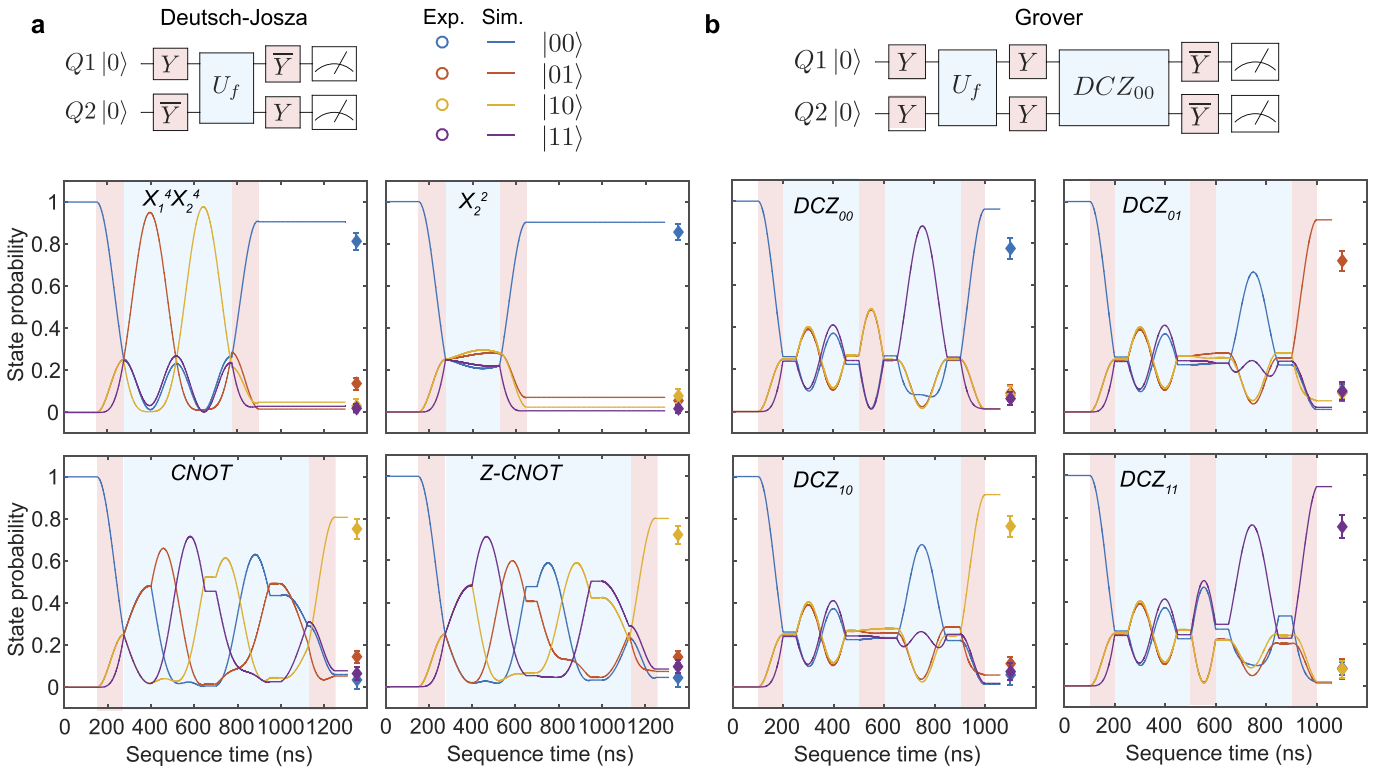

Extended Data Figure 10 | Simulation of the Deutsch–Josza and Grover search algorithms using the DCZ gate. a, **b**, Two-spin probabilities as a function of the sequence time during the Deutsch–Josza algorithm (**a**) and the Grover search algorithm (**b**) for each function, using the decoupled version of the two-qubit CZ gate (the DCZ gate). The solid lines show the outcome of the simulations, which include decoherence due to quasi-static charge noise and nuclear-spin noise. All error bars are 1σ from the mean.